Article published in *J. Med. Chem.* (2018) 61, 5922–5933

DOI: 10.1021/acs.jmedchem.8b00105

https://pubs.acs.org/doi/10.1021/acs.jmedchem.8b00105

Paradoxically, Most Flexible Ligand Binds Most Entropy-Favored: Intriguing Impact of Ligand Flexibility and Solvation on Drug-Kinase Binding

Barbara Wienen-Schmidt[‡], Hendrik R.A. Jonker[†], Tobias Wulsdorf[‡], Hans-Dieter Gerber[‡], Krishna Saxena[†], Denis Kudlinzki[†], Sridhar Sreeramulu[†], Giacomo Parigi[#], Claudio Luchinat[#], Andreas Heine[‡], Harald Schwalbe[†]*, Gerhard Klebe[‡]*

[‡]Institut für Pharmazeutische Chemie, Philipps-Universität Marburg, Marbacher Weg 6, 35032 Marburg, Germany

[†]Institut für Organische Chemie und Chemische Biologie, Johann Wolfgang Goethe-Universität Frankfurt, Max-von-Laue-Straße 7 , N160-3.14 , 60438 Frankfurt am Main, Germany

[#]Magnetic Resonance Center (CERM/CIRMMP) and Department of Chemistry, University of Florence, Via Luigi Sacconi 6, 50019, Sesto Fiorentino, Italy

KEYWORDS: Thermodynamics, Protein Kinase A (PKA), Fasudil, X-ray Crystallography, NMR, ^{15}N-T_2-relaxation time, ($^1H^{15}N$)-TROSY, Degrees of Freedom, Molecular Dynamics Simulation, GIST

ABSTRACT: Considering biophysical parameters in drug design can accelerate the development of clinically successful drugs. Designing rigid ligands can reduce the entropic penalty upon protein target binding, thus improving affinity. Nonetheless, systematic studies are required to demonstrate the impact of ligand rigidification on the thermodynamic binding profile. We studied the effect of ligand flexibility on thermodynamics by binding a series of ligands derived from the approved drug fasudil to cAMP-dependent protein kinase (PKA). The ligands vary in internal degrees of freedom but conserve the atom count and number of heteroatoms. Protein-ligand interactions were scrutinized using X-ray crystallography, isothermal titration calorimetry, nuclear magnetic resonance spectroscopy and molecular dynamics simulations. Four aspects may influence the resulting thermodynamic signature: (1) protein-ligand complex flexibility, (2) ligand flexibility, (3) protein-ligand complex hydration, and (4) ligand desolvation. NMR and crystal structures show no differences in protein-ligand complex flexibility across the series although strong ligand-induced adaptations are observed. Counterintuitively, the most flexible ligand displays the entropically most favored binding, which cannot be explained by higher residual flexibility of the formed complex or an increased release of water upon complex formation. Instead, the flexible ligand entraps more efficiently water molecules in solution prior to protein binding and by releasing these waters the favored entropic binding is observed. Our example demonstrates that understanding and predicting thermodynamic binding profiles will only be successful if properties are systematically varied in series and any step along the binding pathway can be determinant for the overall observed thermodynamic binding profile.

INTRODUCTION:

Finding selective, effective and clinically successful drugs is a long and expensive enterprise. Hence, it would be beneficial to accelerate this process by improving criteria to predict successful drug candidates and to identify inappropriate ones early on. Therefore, the analysis of parameters beyond affinity is required. In this context, thermodynamic analysis of protein-ligand interactions is used with increasing popularity. Accordingly, the design of drugs with certain thermodynamic properties has been described as a promising approach in many articles and reviews.[1-6] Moreover, design guidelines to accomplish purposefully tailored profiles have been intensely discussed, frequently advising the development of rigid, correctly pre-organized ligands in order to influence the entropic penalty upon binding of the ligand to its target.[7-10, 2]

However, there remains a lack of systematic studies that explore correlations between ligand structure, target protein characteristics and thermodynamic signature. From our perspective, it is important to distinguish between the different characteristics of proteins. Particular factors that have to be taken into account are: (1) size, (2) flexibility of the target, and (3) water structures. In this study, we investigated the wide and clinically relevant family of protein kinases. Protein kinases are highly flexible proteins as indicated by the presence of flexible loops in the active site and helix movement upon ligand binding.[11-13] They have been rarely investigated by means of comprehensive thermodynamic characterization. Only ten unique kinases are listed in databases that are specialized for thermodynamic annotations, such as Scorpio[14] and BindingDB[15] (CDK2, ERK1/2, JNK2, Pim1, Aurora-A, Thymidine Kinase, Nucleosid Diphosphate Kinase, vSrc, cSrc). Indeed for none of these targets has a systematic investigation of ligand series been conducted. Considering that according to Manning the human genome might encode for up to 518 protein kinases[16] and with respect to their importance as a drug target class, there is a clear need for thermodynamic data to characterize protein kinases. The aim of this study is to start filling this gap, in order to broaden our understanding of kinase dynamics and thermodynamics of ligand binding.

Here, the use of well-studied model proteins allows for the capture of extensive information from a wide range of experimental techniques. Using the cAMP-dependent protein kinase (PKA) as a model system, elaborate information on protein-ligand interaction was obtained using X-ray crystallography, isothermal titration calorimetry (ITC) and nuclear magnetic resonance spectroscopy (NMR). The selected ligands are derived from the approved drug **fasudil**,[17] which has been developed as a rho-kinase inhibitor[18] but, nonetheless, displays nanomolar affinity toward PKA.[19] All of these ligands have an equal number and scope of atom types of heteroatoms but vary in their internal degrees of freedom (**Figure 1**). In this way, the effect of ligand flexibility on the thermodynamic protein binding profile can be investigated. Thorough analysis of the underlying structural factors contributing to this thermodynamic profile has been made using X-ray crystallography and $^{1}H^{15}N$ best-TROSY (transverse relaxation optimized spectroscopy) NMR spectra. Furthermore, protein-ligand complex dynamics were analyzed using ^{15}N-T_2-relaxation measurements. Further insights about changes in the protein hydration pattern were obtained from water ^{1}H NMRD profiles by measuring the water proton relaxation rates. Here, we present a unique study where the static data from high resolution crystal structures is faced and combined with the information on the dynamics from detailed NMR measurements and molecular dynamics (MD) simulations.

For the thermodynamic data, ITC was used to measure K_D and ΔH. Subsequently, $-T\Delta S$ was calculated using the expression for Gibbs free energy of binding:

$$\Delta G = \Delta H - T\Delta S = RT \ln K_D$$

where ΔG was determined from K_D using the definition of Gibbs free energy for a system at chemical equilibrium.

Our study displays striking results that could hardly have been predicted, as counterintuitively the most flexible ligand binds entropically most favorably to the protein. Consequently, the hypothesis stating that a significant loss of ligand's degrees of freedom is, in all cases, entropically unfavorable to binding, needs to be questioned and analyzed in the context of the entire binding event. We conclude that a generalization of simple design guidelines is not constructive and will not lead to satisfactory results.

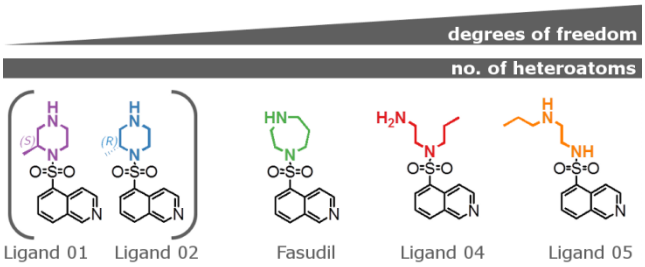

Figure 1. Chemical structure of the five ligands used in this study. From the left to the right the internal degrees of freedom increase and will, in any case, require an entropic price to be paid upon binding, as an increasing number of torsional degrees of freedom will be lost. In purple: *S*-methyl-piperazine substituted fasudil-derivative (Ligand **01**); in blue: *R*-methyl-piperazine substituted fasudil-derivative (Ligand **02**); in green: **Fasudil**; in red: open-chain fasudil-derivative (Ligand **04**); in orange: long-chain fasudil-derivative (Ligand **05**).

EXPERIMENTAL SECTION:

Protein Expression and Purification for ITC and Crystallization. The catalytic subunit of cAMP-dependent protein kinase from Chinese hamster ovary cells (98% sequence idendity with human isoform) was expressed with

a His-tag in a modified pET16b-Vector with an introduced TEV-cleavage site between the protein N-terminus and His-tag. This plasmid was transformed into *E. coli* strain *Bl21 (DE3)/pLysS* (Novagen).[20]

Cell disruption was performed using a high-pressure homogenizer for multiple cycles. After centrifugation (1h at 30.000g) cell lysate supernatant was purified in a first step using a Ni-NTA column that binds the His-tag of the protein and was eluted by an imidazole gradient. The His-tag was then cleaved off by TEV-protease. Afterwards, an inverse Ni-NTA column was employed collecting PKA in the flow-through. Finally, ion exchange chromatography was performed using a MonoS column separating three-fold phosphorylated PKA from the four-fold phosphorylated form using a HEPES buffer with a sodium chloride gradient.[20]

Protein Expression and Purification for NMR. The catalytic subunit of cAMP-dependent protein kinase was expressed, isotope labeled (N^{15}) and purified as previously described.[21]

Crystallization. Co-crystallization was performed using the hanging drop method at 4 °C. The crystallization drops were composed as follows: 10 mg/mL PKA (240 µM), 30 mM MBT (MES/Bis-Tris buffer pH 6.9), 1 mM DTT, 0.1 mM EDTA, 75 mM LiCl, 0.03 mM Mega 8, 0.07 mM PKI (Sigma: P7739), 1.2 mM ligand dissolved in DMSO from a 50-100 mM stock. The well contained a mixture of methanol in water with varying methanol concentrations (v/v) for the different ligands (**fasudil**: 18% methanol; Ligand **05**: 18% methanol; Ligand **04**: 14% methanol; Ligand **01**: 16% methanol; Ligand **02**: 19% methanol). In the crystallization setup streak-seeding was performed using a horse hair in order to initialize crystal growth. For crystal mounting, crystals were cryo protected in 5 mM MBT (MES/Bis-Tris buffer pH 6.9), 1 mM DTT, 0.1 mM LiCl, 1.2 mM ligand dissolved in DMSO from a 50-100 mM stock, 16 % (v/v) methanol, 30% (v/v) MPD and flash frozen in liquid nitrogen.

Crystal Structure Determination. All structures were collected at the storage ring Bessy II Helmholtz-Zentrum Berlin, Germany at Beamline 14.1 on a Pilatus 6M pixel detector. The datasets were processed using XDS[22] and molecular replacement was performed using CCP4 Phaser[23] and PDB-structure of PKA from *bos taurus* 1Q8W as a model.[19] This was followed by simulated annealing, multiple refinement cycles of maximum likelihood energy minimization and B-factor refinement using Phenix.[24] Coot[25] was used to fit amino-acid side chains into σ-weighted $2F_o - F_c$ and $F_o - F_c$ electron density maps. If appropriate electron density was observed, multiple side chain conformations were built into the model and maintained during the refinement if the minor populated side chain displayed at least 20 % occupancy. Hydrogen atoms were included using a riding model. Ramachandran plots for structure validation were calculated using PROCHECK.[26] Data collection, unit cell parameters and refinement statistics are given in the supplementary information (**Table S2**). Analysis of temperature factors was performed with Moleman.[27] Protein and PKI B-factors were anisotropically refined, water B-factors were isotropically refined for all structures. R_{free} was calculated using 5% of all reflections which were randomly chosen and not used for the refinement. The required ligand restraint files were created using the Grade webserver.[28, 29] For figure preparation Pymol was used.[30]

Isothermal Titration Calorimetry. The buffer used for the ITC experiments contained: 30 mM sodium phosphate buffer pH 7.2, 10 mM MgCl2, 100 mM NaCl, 3% (v/v) DMSO. All measurements were repeated 3-5 times. Further buffers were used in order to check for protonation linkage. In these buffers 30 mM sodium phosphate buffer was replaced by 30 mM HEPES and 30 mM triethanolamine (TEA), respectively (both at pH 7.2). Buffer dependency was tested for all measurements in the absence of PKI. For the measurements expressed, purified and dialyzed PKA was used in the ITC-measuring cell. A 15-20 fold higher concentrated ligand solution, diluted in dialysis buffer, was then stepwise injected to the protein solution during the measurement. All measurements were performed at 25 °C. ITC data were analyzed using NITPIC and Sedphat.[31, 32] Raw data and exact values and standard deviations for ΔG, ΔH and −TΔS can be found in the supplementary information (**Table S3, S4**).

Compound purity was analyzed using quantitative nuclear magnetic resonance spectroscopy (qNMR) and in case of deviation, ligand concentration was corrected accordingly.

NMR Measurements. The NMR samples contained about 0.1-0.2 mM PKA protein, 20 mM sodium phosphate buffer (pH 6.5), 80 mM NaCl and 2 mM TCEP (tris(2-carboxyethyl)phosphine) and 10% D2O (for spectrometer lock). The NMR experiments were conducted at a temperature of 298 K on Bruker Avance 600, 800 and 950 MHz spectrometers equipped with cryogenic triple-resonance probes. For the PKA+PKI complex, titration experiments were performed in which the unlabelled PKI peptide was added until no significant changes were observed anymore in the $^1H^{15}N$-HSQC spectra after the last addition. The samples of PKA with PKI contained a slight excess of the PKI peptide and the samples with the ligands contained a 5 times excess of the ligand to assure the full complex formation. NMR spectra were acquired and processed using Topspin version 3.2 (Bruker Biospin) and analyzed using Sparky 3.114 (T. D. Goddard and D. G. Kneller, University of California, San Francisco). Resonances for the PKA protein have been assigned before[21, 33]. The spectra of PKA alone, PKA with PKI, PKA with ligands and PKA with PKI and ligands have been assigned by overlaying the $^1H^{15}N$-HSQC spectra. Only the backbone amide signals that could be tracked reliably were further analyzed. Heteronuclear ^{15}N-T_2 relaxation experiments were performed on the uniformly ^{15}N labeled PKA protein in complex with PKI with and without ligands. The relaxation rates were determined from a series of spectra with delays of 0, 16.96,

33.92, 50.88 and 67.84 ms. The amide chemical shift perturbations (CSPs) were acquired from $^{1}H^{15}N$-best-TROSY[34] spectra.

Relaxometry. Water ^{1}H NMRD profiles were obtained by measuring the water proton relaxation rates, R_1, as a function of the applied magnetic field. The NMRD profiles were measured with a SPINMASTER2000 fast field cycling relaxometer (Stelar, Mede (PV), Italy) operating in the 0.01–40 MHz proton Larmor frequency range, at 298 K. The measurements are affected by an error of about ±1%, when fitted to a monoexponential decay/recovery of the magnetization in the field cycling experiment. Measurements were performed either in the presence or in the absence of PKI, with and without **fasudil** and with and without ligand **05**. Protein concentrations were 0.5 mM and 0.21 mM in the absence of PKI, and 0.5 mM when PKI was added. Ligand concentration was 4-6 times larger than the protein concentration.

The profiles were fit using Eq. (1), where protons are assumed in fast exchange and the model-free model is applied:

$$R_1=(0.3+a)+ b_1J(\tau_{slow})+b_2J(\tau_R)+b_3J(\tau_{fast}) \quad (1)$$

with $J(\tau)=0.2\,\tau/[1+(\omega\tau)^2]+0.8\,\tau/[1+(2\omega\tau)^2]$ and where a, b_1, b_2, b_3, τ_{slow}, τ_R, τ_{fast} are fitting parameters. In order to reduce the covariance among the many fit parameters, all profiles were fit simultaneously by imposing common values for τ_{slow}, τ_R and τ_{fast} in the absence of PKI, and τ_R and τ_{slow} values 5.4% larger in the presence of PKI (due to the estimated slower reorientation time of the complex upon PKI binding).

Ligands. Ligands **01**, **04** and **05** were purchased from Uorsy (Ukraine). The *R* and *S* isomers of the 2-methylpiperazine inhibitors **01** and **02** were synthesized starting from 5-(chlorosulfonyl) isoquinoline-hydrochloride, prior to this freshly prepared from isoquinoline-5-sulfonic acid via a known literature procedure,[35, 36] which was reacted with the respective, commercially available, enantiomerically pure *R* or *S*-configured mono-N-Boc-protected 3-methylpiperazine thus rendering the corresponding inhibitor precursors, respectively. Finally, N-Boc deprotection with 4 M HCl in dioxane gave rise to the corresponding inhibitors **01** and **02** as their hydrochloride salts.

RESULTS

Strongest induced fit is triggered by the most flexible ligand. In order to determine the binding modes of all five ligands discussed, co-crystal structures were obtained. For all structures, resolutions between 1.4 and 1.6 Å could be achieved. In all five cases, difference electron densities are well defined and indicate every heteroatom of the bound ligands (supplementary information, **Table S1**) with 100% occupancy in the binding site. All structures have been deposited in Protein Data Bank (PDB). The respective codes are listed in

Table 1.

Table 1. List of PDB-codes for the different ligand co-crystal structures

Ligand	PDB code
Ligand 01	5LCU
Ligand 02	5LCT
Fasudil	5LCP
Ligand 04	5LCR
Ligand 05	5LCQ

Importantly, the crystallographic data confirmed that all five ligands display a congruent hinge binding position of their respective isoquinoline moiety (**Figure 2B**). Moreover, their adjacent sulfonamides occupy a common orientation in all structures, where one oxygen points toward the Glycine-rich loop (Gly-loop) and the second toward the hinge region. Hence, protein-ligand interactions are highly similar for the isoquinoline-5-sulfonamide portions of all five ligands. In all structures, a hydrogen bond is formed between the isoquinoline-nitrogen of the ligands and the backbone nitrogen of Val123 of the protein. Besides these interactions, the compounds' sulfonyl-groups do not directly interact with the protein.

In contrast to the very similar ligand core binding, significant changes were noted amongst the five different protein-ligand-complexes considering the attached sulfonamide substituents.

In particular, the αG helix, the APE motif and the position of the protein-kinase-inhibitor-peptide (PKI) are visibly shifted (**Figure 2A**). Yet, the most prominent difference was revealed in the active site. Here, the Gly-loop adopts three distinct positions ranging from a wide-open to a closed conformation when compared to the apo-protein (**Figure 2B)**.

The first, most open position of the Gly-loop exhibits the structure with the open-chained ligand **04** (red). Here, the loop is pushed out of the ligand-binding site as the result of steric hindrance. The binding of ligand **04** simply requires more space in the area of the Gly-loop than any of the other ligands.

The second, half-open conformation of the Gly-loop is found in the structures of *S*-methyl-piperazine substituted ligand **01** (purple), the *R*-methyl-piperazine substituted ligand **02** (blue) and **fasudil** (green). Interestingly, all three ligands share a common position of the Gly-loop even though the interaction pattern of the homopiperazine moiety and 2-methyl-piperazine moieties of the ligands

with the protein differ significantly as will be described later.

Finally, the third, closed state is depicted in the structure of the long-chain ligand **05** (orange). A strong induced fit resulting in a pulling-down of the Gly-loop can be observed. Responsible for this rearrangement are two hydrogen bonds formed between the backbone oxygen of Thr51 and the sulfonamide-nitrogen as well as the secondary amine in the long chain of the ligand as shown in **Figure 2C**. Only in ligand **05** is a secondary amide present in the sulfonamide position and it can hence act as a hydrogen-bond donor. All other ligands possess a tertiary amide as an equivalent, which does not have the ability to act as a hydrogen-bond donor. Consequently, the formation of the key interaction to Thr51 is impossible for all other compounds. In addition, steric hindrance would prevent the closed position of the Gly-loop for all ligands other than ligand **05**.

In the case of ligand **05**, the closed conformation of the Gly-loop is facilitated by additional interactions of the loop involving the following amino acids of the protein: Asp184, Ser53 and Lys72. In total, five new interactions are formed (**Figure 2C**, black dotted lines).

From further analysis of the ligand binding mode, differences can be discerned with respect to the deviating substituents (**Figure 3**). The interaction patterns established by the terminal amines differ. The highest number of polar interactions to the protein is recognized by the homopiperazine portion of **fasudil** (green) and the terminal aminoethyl moiety of the open-chain ligand **04** (red). Interestingly, both ligands form comparable interaction patterns. In either case, the terminal amino group forms hydrogen bonds with the backbone carbonyl oxygen of Glu170 as well as the terminal carboxamide or carboxylate group of the side chains of Asn171 and Asp184. In contrast to **fasudil** (green) and **04** (red), the interaction pattern of the terminal aminoethyl nitrogen of the long-chain ligand **05** (orange) differs. The only common interaction occurs with the backbone carbonyl oxygen of Glu170. Furthermore, **05** interacts with the side chain of Glu127.

It is also notable that the *S*-methyl-piperazine substituted **01** (purple) and the *R*-enantiomer **02** (blue) each establish one hydrogen-bond to Asp184 of the DFG-loop via their terminal NH group.

A difference in the position of water molecules of the residual hydration pattern can be observed for the different complexes. As a matter of fact, the protein flexibility takes impact on the observability of the adjacent water positions. By optimizing the diffraction quality of the studied crystals, the resolution of the collected datasets was improved. Nonetheless, many putative water molecule positions remained unresolved due to an ambiguous density distribution next to the region showing enhanced residual mobility in the crystal structure. A distinct analysis and quantification of the water molecule pattern and hence a comparison across the active sites of all complexes is limited due to the flexible nature of the protein, which affects the diffraction pattern defining the electron density in this region.

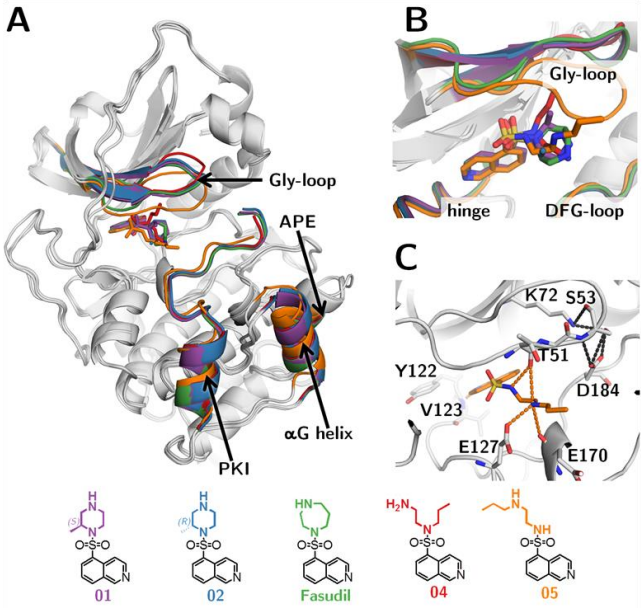

Figure 2. Superimposition of the co-crystal structures of all five ligands. **A**: Overall view of the protein. Ligand **01** is displayed in purple; **02** in blue; **fasudil** in green; **04** in red and **05** in orange. **B**: Blow up of the active site. The long-chain ligand **05** induces the strongest conformational change dragging the Gly-loop toward the ligand. **C**: Interactions between **05** and the protein are displayed as orange dotted lines. The key interaction responsible for the downward movement of the Gly-loop is a hydrogen bond to Thr51. This transition is facilitated by the new interactions formed by the Gly-loop to the remaining part of the protein. The latter contacts are displayed as black dotted lines.

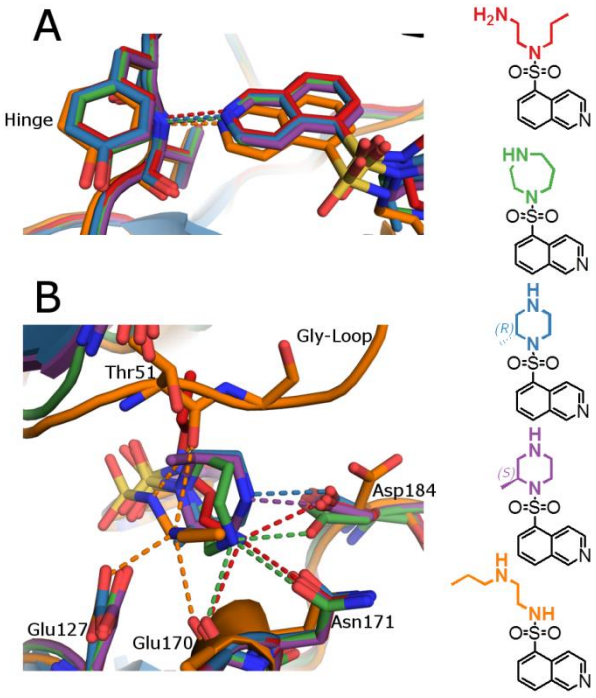

Figure 3: Polar interactions of all five ligands to the corresponding protein structures. Ligand **04** is displayed in red; **fasudil** in green; ligand **02** in blue; ligand **01** in purple and ligand **05** in orange. Polar interactions are represented as dotted lines and colored in conformity with the corresponding ligand. **A:** Interaction of the isoquinoline with the hinge region of the protein. **B:** The different polar interactions of the five ligands additional to those shown in A.

The most flexible ligand binds entropically most favored to the protein. The thermodynamic signature of ligand binding to the protein was determined by ITC. All profiles were assessed for putative buffer dependence. No significant protonation effects were observed. The selected buffers differ in their ionization enthalpy by approximately 30 kJ/mol.[37] A slope between -0.07 and -0.15 could be observed for **01**, **05** and **04**, across the three considered buffers, a value considered as insignificant. For **01** and **02**, a slope of +0.15 was revealed. The calculated pKa value for the piperazine nitrogen is 7.3, which is slightly below the applied buffer pH (calculated using http://www.chemicalize.org/). Hence, there might be a slight protonation effect, owing to a partial proton uptake, in particular if compared to the slopes of the other compounds, which have calculated pKa values between 8.0 and 10.1. However, also this amount of proton uptake is still close to the significance threshold. Nonetheless, the profiles used for the evaluation of the thermodynamic signatures were determined in phosphate buffer to profit from the very low ionization enthalpy of this buffer. In literature, values ranging from 0.93 to 5.12 kJ/mol were reported as heat of ionization for the phosphate group.[37]

To reveal a closer match with the crystallographic data we applied two distinct scenarios during the ITC titrations, both potentially important under physiological conditions. In the first set of titrations, the ligand was directly titrated to the protein in the sample cell. In the second set of titrations, an alternative strategy was used: A peptide sequence of the substrate protein to be phosphorylated was added to the protein in the sample cell. In our experiment, a 20 residue peptide named PKI was applied. It is assumed that this peptide binds at the same position in the active site, adjacent to the ATP-binding site, as the substrate proteins. PKI mimics the amino acid sequence motif of the substrate proteins exhibiting as only difference the replacement of the Ser/Thr residue that becomes phosphorylated by an Ala.

Accordingly, measurements were performed in the presence (squared symbols) and absence (circular symbols) of the substrate-mimicking inhibitor peptide PKI (**Figure 4**).

Upon comparison of the relative differences of the two sets of thermodynamic profiles, it is apparent that on an absolute scale an offset between the sets of profiles is given leading to a shift toward more favorable entropy and less beneficial enthalpy in the presence of PKI (squared symbols). Thus, the relative differences between the ligands correlate in both cases and the ligands bind with equal potency.

Moreover, it is striking that the binding signatures of **fasudil** (green), the two methyl-piperazine substituted **01** (purple) and **02** (blue) as well as the open-chain ligand **04** (red) are similar and scatter maximally in ΔΔH=4.2 kJ/mol and −TΔΔS=7.8 kJ/mol. In comparison, the long-chain ligand **05** (orange) displays a unique thermodynamic profile significantly reduced in its enthalpic and simultaneously enhanced in its entropic contribution to binding. In consequence, **05** was the most entropically and least enthalpically favorable binding ligand. In case of the presence of PKI, the effect concerning ligand **05** is similar, however, somewhat less pronounced.

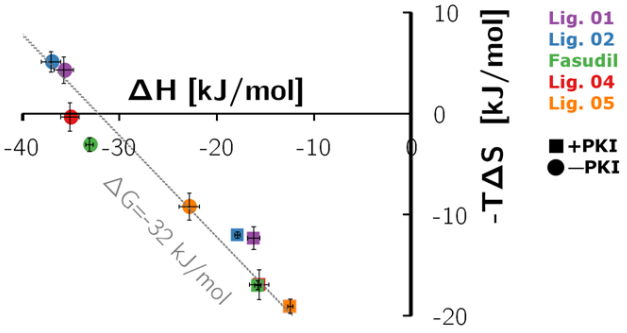

Figure 4. Thermodynamic profiles for all five ligands in absence (circles) and presence of PKI (squares). Entropy is displayed on the Y-axis and enthalpy on the X-axis. The dotted line represents iso-affinity for the mean ΔG values of 32 kJ/mol. Titrations with the different ligands are colored according to the color-code presented in **Figure 1**.

The squared symbol for ligand **04** (red) is virtually hidden as the same profile is found as for **fasudil** (green).

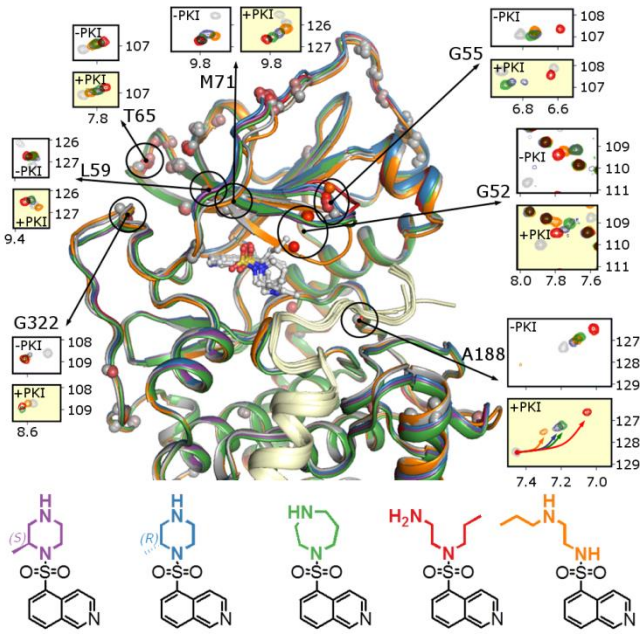

Figure 5. Amide chemical shift perturbations for a selection of residues and their corresponding location in the X-ray crystal structure. Sections from an overlay of $^{1}H^{15}N$-best-TROSY spectra are shown from PKA with and without ligands in the presence and absence of the PKI-peptide.

Correlation of amide chemical shift perturbations in presence and absence of PKI. To further analyze the structural influence of the peptidic inhibitor PKI, which is present in all of the studied crystal structures, $^{1}H^{15}N$ best-TROSY spectra of PKA were measured and the amide chemical shift perturbation (CSP) of 88 amino acids were determined for each ligand in the presence and absence of PKI (**Figure S6A-C**). **Figure 5** shows the CSP for a selection of residues in the absence and presence of PKI for the five different ligands and the corresponding amide location in the X-ray structure. These data indicate similar binding properties of the ligands either in absence or presence of the PKI peptide and thus demonstrate the relevance of the crystal structures only determined in presence of PKI.

The largest spatial difference can be observed for residues Gly55 (not assignable for the long-chain ligand **05**), Ala188 and Arg256 (**Figure S6D**). Gly55 is located in the Gly-loop, which is involved in the strongest induced-fit adaptations among the five crystal structures. Ala188 resides two amino acids C-terminal from the DFG-motif and is in close proximity to the PKI-peptide's C-terminus. Arg256 is remote from the active site at the bottom of the large subunit located in close proximity to the N-terminus of the PKI peptide. The NMR data fully support and agree with the structural information from crystallographic analysis. The structural alignment of the crystal structure in **Figure 2** was performed using the backbone atoms of the residues with the smallest CSPs, thereby ensuring an unbiased alignment.

The most flexible ligand does not form a flexible protein-ligand complex. In order to analyze the residual flexibility of the resulting protein-ligand complexes ^{15}N-T_2-relaxation NMR measurements were performed. These data (**Figure S6D**) indicate higher flexibility for the N-terminal 13 residues. The average of the remainder ^{15}N-T_2 relaxation values (75 of the 88 backbone amide signals that could be tracked reliably) are presented in **Figure 6**. The ^{15}N-T_2-relaxation time can be used as a measure for backbone dynamics (a more rigid protein backbone will show a smaller ^{15}N-T_2 relaxation time). On average, the dynamics of all five complexes are very similar. Interestingly, ligand **05** with the largest amount of internal degrees of freedom does not form a significantly more flexible protein-ligand complex compared to the other more constrained members of the series.

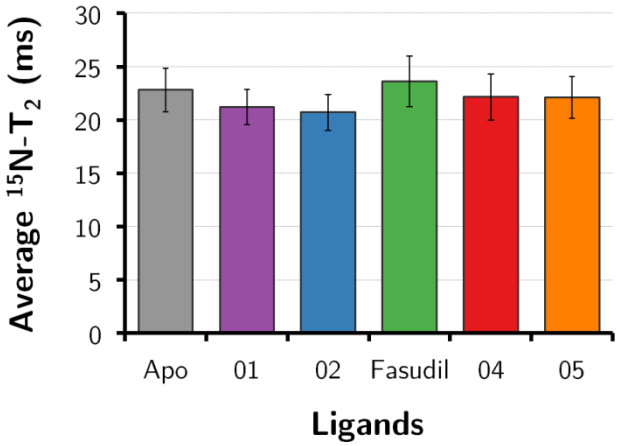

Figure 6. The average amide ^{15}N-T_2-relaxation time for the PKA protein (75 out of 88 residues, excluding the flexible N-terminal residues) in presence of the PKI peptide, with and without ligands. The overall differences are small. Error bars present the averaged standard deviation.

Protein hydration with and without fasudil or ligand 05. Relaxometry measurements were performed at 298 K for PKA with and without the inhibitor peptide PKI and/or with and without **fasudil** (**Figure 7**). The data show that in the presence of PKI and/or **fasudil** the relaxation rates are slightly larger than for the free PKA samples. Furthermore, while the relaxation rates are basically constant at low fields in the presence of PKI and/or **fasudil**, the profiles for the free PKA samples show a slight decrease between 0.1 and 1 MHz. Consequently, the relaxometry profiles measured in the presence of PKI/**fasudil** can be nicely reproduced from the sum of two Lorentzian dispersions with different correlation times, whereas the profiles of free PKA require three Lorentzian dispersions. All profiles were thus fitted using Eq. 1, and the best fit

values are found in **Table S5**. Water molecules interacting with the protein or with the protein complexes as well as exchangeable protein protons contribute to the observed relaxation rates depending on the correlation time modulating the dipole-dipole interactions. The effective correlation time for the different protons is the fastest between the reorientation time and the exchange time. The parameter a reports on the contribution to water relaxation from protons relaxing with correlation times smaller than few ns, whereas b_1, b_2 and b_3 report on the contributions from protons relaxing with correlation time τ_{slow}, τ_R (the protein reorientation time) and τ_{fast}, respectively, with τ_{fast} shorter than τ_R but larger than few ns. This correlation time can either be due to fast local mobility at the protein site or to a water exchange rate faster than protein rotation. The contribution from protons relaxing with such a correlation time much shorter than τ_R is typically between 40% and 80% of the total.

This fit shows that the contribution from protons relaxing with a correlation time τ_R = 28 ns or with a correlation time τ_{fast} = 5 ns slightly increases on passing from free PKA to PKA bound to PKI and/or fasudil, whereas the small amount of protons relaxing with a correlation time τ_{slow} =240 ns decreases. The best fit value of τ_R (28 ns) is in good agreement with the value calculated with HYDRONMR using the PDB structure 4WIH[20], for which a correlation time of 26 ns is calculated. The presence of a decreased contribution from water molecules with correlation time τ_{slow} upon PKI and **fasudil** binding may suggests that in free PKA some aggregation is present, and that the aggregated protein decreases/disappears in the presence of the ligands. Overall, the data indicate that the hydration of the protein does not decrease, but rather slightly increases upon PKI and/or **fasudil** binding, although the difference is close to the error of the best fit values.

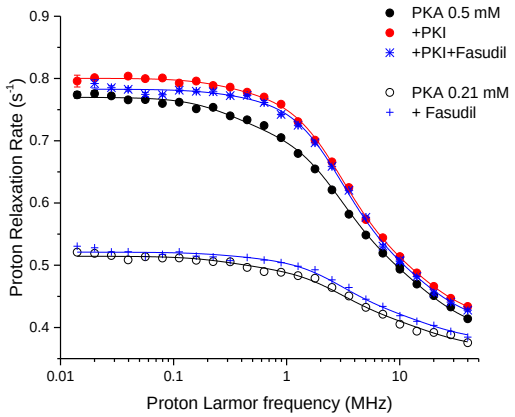

Figure 7. Water proton relaxometry profile of PKA with and without PKI and/or **fasudil** at 298 K. The lines are the best fit profiles calculated from the parameters reported in **Table S5**.

In addition, we investigated whether relaxometry could detect differences between the binding of **fasudil** and ligand **05** as a result of a larger number of water molecules removed from the active site upon ligand **05** binding than upon **fasudil** binding. This could explain the entropic advantage found for **05** binding to PKA. We therefore collected relaxometry profiles of PKA in presence and absence of PKI with either ligand **05** or **fasudil** (**Figure S7**). These measurements show, however, that no differences can be detected between PKA+**fasudil** and PKA+ligand **05**.

Entropic desolvation contributions investigated by molecular dynamics simulation. In order to obtain insights about the molecular contributors to entropy on atomic resolution, molecular dynamics (MD) simulations were carried out, specifically for **fasudil** and **05**. Simulations were conducted for these ligands bound to PKA as well as in solution (unbound state). The study proceeded with an in-depth analysis of the ligand desolvation thermodynamics (see Supporting Information). Finally, these results were faced to and validated by experimental NMR NOE data.

Ligand configurational entropy paradigm confirmed by simulation. Initially, MD simulations of **fasudil** and **05** were conducted in their protein-bound state (each 50 ns) as well as in their unbound solution state (each 100 ns). Subsequently, the configurational entropy difference is calculated using *CENCALC*[38] for each of the two ligands in their bound and unbound state. As anticipated by their chemical composition, the loss in binding due to the configurational binding entropy contribution ($-T\Delta S_{conf}$) for **05** is larger than for **fasudil** (**05:** 31.65 kJ/mol, **fasudil**: 8.41 kJ/mol, see Table 2.1 in SI). Since NMR spectroscopy revealed no structural perturbation of the protein upon binding, the subsequent evaluation has solely been focused on the internal degrees of freedom of the ligands **fasudil** and **05** and those of the protein have been omitted in the calculations.

Calculation of ligand desolvation entropy. The trajectories obtained from unbound 100 ns MD simulations of **fasudil** and **05** were clustered with the hierarchical agglomerative average-linkage implementation of *cpptraj* (V15, see section 6.3.1 in SI). The **fasudil** ensemble was found to be well described by two, equally populated, conformational clusters. In contrast, geometrical variance of **05** was best described using three clusters. Most interesting, the crystallographically adopted conformation of the bound state is found in the least populated cluster (13.9%). The cluster centroids were then used as starting structures for new MD simulations with positional restraints, such that the conformations of the cluster centroids were preserved throughout the simulations. Removal of internal degrees of freedom is important for subsequent GIST[39, 40] post-processing. In GIST, several solvation thermodynamic quantities, such as entropy, are mapped on a three dimensional grid.

Visual inspection of the GIST entropy maps revealed that the secondary amino group is well solvated for both, **fasudil** and **05** (**Figure 8**). The desolvation of that group would be entropically beneficial, since solvent hydrogen-bonding interactions result in both, translational and orientational restrictions of the entrapped water molecules. On the contrary, the sulfonamide nitrogen atom is less well solvated in **fasudil** (**Figure 8**(A)) compared to **05** (**Figure 8**(B)). This is probably enhanced by the predominant *pseudo*-macrocyclic back-folded shape of **05**, which increases the barrier of the sulfonamide-bound water molecules to exchange with bulk solvent. Consequently, the desolvation entropy of the sulfonamide nitrogen is expected to be significantly more negative in the case of **05**.

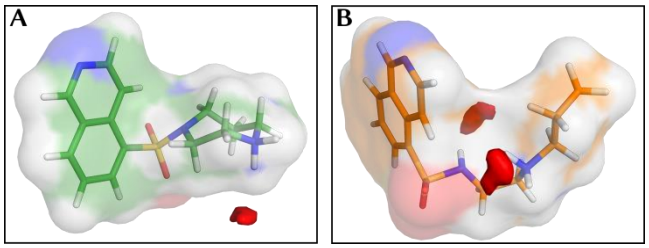

Figure 8. **A: Fasudil** and **B: 05** in their cluster centroid conformation found for the main clusters. The red isosurface displays solvent entropy at -2.5 kJ/mol/Å3.

Some total solvation quantity (in relation to bulk solvent), ΔA^0, is obtained from GIST calculations of several (representative) conformations using the following equation:

$$\Delta A^0 = \int_{q_0}^{q_N} p(q) \cdot \Delta A^0(q)\, dq \qquad (2)$$

Here, *p(q)* is the probability to find the solute in conformation *q*, *p(q)* is the cluster occupancy and *q* is a cluster centroid conformation. The change in solvation entropy in the vicinity of the solute can be accessed quantitatively by spatially integrating the entropy map over a volume near the surface of the ligand (background on the method is found in section 1.4 of the SI).

Table 2. Different solvation thermodynamic properties, ΔA, as obtained from GIST. The uncertainty reported for each value is the ±standard deviation from the mean.

ΔA [kJ/mol]	**fasudil**	**05**	**Δ**
$-T\Delta S_{orient}$	41.58±0.04	48.06±0.34	6.48±0.34
$-T\Delta S_{trans}$	53.55±0.34	62.26±0.21	8.71±0.37
$-T\Delta S_{tot}$	95.12±0.63	110.32±0.38	15.20±0.71
ΔE_{ww}	360.36±5.95	367.81±4.10	7.45±7.20
ΔE_{sw}	-329.12±1.37	-343.90±3.64	-14.78±6.78
ΔE_{tot}	31.11±8.25	23.95±5.48	-7.16±9.92
ΔG	126.40±8.29	134.27±5.49	7.87±9.92

Due to the enhanced hydrogen bonding properties of the sulfonamide group in **05**, increased solvation entropy contributions are suggested in comparison to **fasudil** (**Table 2**). A difference in $-T\Delta S_{tot}$ at 300 K between the two compounds is computed as 15.20 ± 0.71 kJ/mol. With respect to the solvation free energy no significant difference between both ligands can be assigned, mainly due to error propagation of the large individual energy contributions.

Combined NMR and MD experiment. The water molecules trapped by **05** in its unbound conformations cannot be characterized by the NMR experiment directly, due to the fast exchange rate of ligand-trapped water molecules. It is assumed that the solute perturbs the otherwise homogenous solvent and therefore gives rise to enhanced solvent structuring. Following that rationale, the match of the *in silico* ensemble with an experimental ensemble would strongly indicate that the proposed solvent structuring takes place in solution and leads to the above computed favorable solvation entropy. For this purpose, an MD simulation of **05** in water is carried out using NMR-derived distance potentials.

Initially, the NOE distances were transformed into (parabolic) distance potentials for MD simulations. In total 36 MD simulations with differing of distance potentials settings for distance potential calculation and varying force constants were carried out. After obtaining the trajectory that agreed best with the experimental data (see section 6.52. in SI), its principal component (PC) subspace overlap with the main cluster obtained from the initial simulation was calculated.

The trajectory that agreed most with experimental data (91% within experimental boundaries) was generated using a set of $\langle d_{ij}^{-6} \rangle^{-1/6}$ distance potentials. Based on this trajectory, a principlal component (PC) subspace overlap of 0.51 is found with the *in silico* ensemble (section 6.5.3 in SI), which is quite high given the high dimensionality of the configuration space compared to the PC subspace. Since subspace overlap can be obscured by different effects, the significance of the result was further assessed by its Z-score[41]. The Z-score is constructed by comparing the actual overlap to the overlap with a background model consisting of 500 random trajectories. Positive values indicate high significance, zero or negative values indicate insignificant overlap. The calculated Z-score in the present case is 5.84, and therefore indicates that similarity between the experimental ensemble and the *in silico* main cluster of **05** is far above noise and therefore can be assumed significant.

DISCUSSION:

For a series of five congeneric and nearly equipotent ligands, studied in this contribution, we thoroughly analyzed the interactions with PKA. High-resolution crystallographic data revealed a comparable hinge binding mode of all ligands. As special feature a strong induced-fit mechanism for ligand **05** (orange) is observed. NMR chemical shift perturbation data reveals high similarity between the structural properties of the different complexes in crystalline and solution state as similar shifts can be observed in the presence and in the absence of the inhibitor peptide PKI from the crystallization condition. NMR relaxation time measurements unraveled the structural influence of PKI on the protein and allowed analysis of the backbone dynamics, which however, agree across all studied complexes. Thermodynamic signatures were measured either in the absence or in the presence of the substrate mimicking peptide PKI. Even though all ligands bind with nearly the same affinity, they distinctly factorize in enthalpy and entropy. This also uncovers that ligand **05** is, on first sight paradoxically, the most entropically favored binder of the series, independent of the presence or absence of PKI.

On first sight, it appears quite counterintuitive that the long-chain ligand **05** (orange) exhibiting the largest amount of internal degrees of freedom, is the most entropically favored binder in the presence as well as absence of PKI. Usually, the binding of more rigid and conformationally preorganized ligands reveals an entropic advantage to binding.[42, 43] In the present case, this would be expected for the ligands **fasudil**, **01** and **02** possessing the conformationally restricted cyclic substituents.

It is remarkable that the relative differences in the thermodynamic profiles between the five ligands remain similar with and without the substrate-like PKI. However, the overall shift of all profiles on absolute scale toward more entropy-favored binding appears reasonable upon binding of the substrate peptide as the protein becomes prestabilized and structurally organized in a way to better recognize either the co-substrate ATP or, in our case, the inhibitors of the fasudil-type. The thermodynamic profiles of ligand binding are all shifted toward an entropically more favorable but enthalpically less beneficial signature in the presence of PKI. This profile is in accordance with a better preorganization of one of the binding partner, here of the recipient protein.

Among the individual ligands, the entropically more favored binding of ligand **05** to PKA could result from (*i*) the formation of a protein-ligand complex with strongly enhanced residual flexibility, (*ii*) from increased displacement of active-site water molecules upon ligand binding to the uncomplexed protein, or (*iii*) from a difference in the solvation properties among the five ligands in aqueous solution prior to binding. These contributions must even overcompensate the entropic losses to be paid by restricting the conformational flexibility of ligand **05** to the bound state. The first aspect appears unlikely, as ligand **05** shows overall the lowest B-factors in the crystal structure, thus the lowest residual mobility in bound state (**Table S2**) and a strong induced-fit adaptation, pulling the Gly-loop towards the bound state. Furthermore, NMR relaxation data do not indicate any deviating behavior for this ligand. Clearly, these findings do not speak for an entropic advantage of **05** upon binding. Another possible explanation for the favorable entropy contribution of ligand **05** can originate from the displacement of a larger amount of previously well-ordered water molecules upon protein-ligand complex formation. Unfortunately, the amount of water molecules in the active site cannot be reliably evaluated for the entire series by crystallography due to a less-well defined electron density in that area in consequence of enhanced loop flexibility. However, NMR relaxometry measurements, performed for **05** and **fasudil**, suggest that there is no significant difference in the hydration pattern of both protein-ligand complexes. Thus we believe that also differences in the amount of displaced water molecules cannot explain the entropic advantage of the more flexible ligand **05**.

An alternative additional contribution influencing the thermodynamic signature of ligand **05** compared to the other members of the series can arise from differences of the ligands in aqueous solution prior to binding. Remarkably, this effect has nothing to do with the actual protein binding. Once the ligands are released from the bulk water phase and accommodate in the protein, they have to shed their solvation shells. If these shells show structural differences in the local hydration pattern, deviating thermodynamic signatures will result. Indeed MD simulations strongly indicate that the more entropic signal of **05** is due to a unique hydration pattern triggered by a special conformation that favorably entraps water molecules. The frequent occurrence of this conformation was confirmed within the boundaries of NMR spectroscopic data measured for the separately solvated ligand.

Our experimental data demonstrate that the entropically more favored binding of **05** to the protein mainly results from an entropic benefit of the ligand while shedding its hydration shell upon leaving the bulk water phase. Our hypothesis that a ligand with a larger amount of internal degrees of freedom does not necessarily lead to entropically less-favored binding was also observed in other cases, however, without providing a conclusive explanation.[44] Therefore, the assumption that the number of the ligand's degrees of freedom to be lost upon complex formation has a dominating impact on the entropic binding component needs to be questioned or at least requires a more detailed analysis of the binding event as a whole. It demonstrates that simple design guidelines cannot be generalized unreflectively and deserve a much more careful consideration. In particular the frequently neglected factor of ligand solvation has to be more thoroughly considered.

CONCLUSION:

Commonly applied design guidelines need to be systematically investigated and assessed for different protein and ligand classes. Rules that hold for small and rigid proteins do not necessarily apply for larger or flexible proteins. From our systematic study on a protein kinase we conclude that the thermodynamic profile is not dominated by the loss of degrees of freedom due to fewer rotatable bonds on the ligand. The hypothesis that ligand rigidification necessarily results in significantly more entropic binding profiles could not be confirmed. Strikingly, we even recorded the opposite trend in that the most flexible ligand was the most favored entropic binder. Therefore, the loss of degrees of freedom of the ligand, which, as a matter of fact, has to be paid, does not necessarily dominate the thermodynamic profile. Even in the present case of binding to a flexible protein like a kinase, the effect of residual flexibility of the formed protein-ligand complex appears to be minor as all complexes under consideration show very similar NMR relaxation data. In fact, the predominant effect seems to result from structural differences in the hydration pattern of the ligands in the bulk water phase prior to any protein binding. They appear to determine the resulting entropically more favored binding signal.

In summary, our results indicate that the complexity of structure-activity relationships increase with protein flexibility and desolvation differences of either the active site or the ligand molecules. Most strikingly, these contributions cannot be treated as orthogonal design parameters in rational optimization of potential drug candidates. Our data signalize that global understanding and reliable predictions of thermodynamic profiles need a comprehensive view on the binding event and require many more systematic studies of congeneric ligand series.

ASSOCIATED CONTENT

Supporting Information.
The following is supplied as Supporting Information:
Crystallographic tables; pictures of the mF_o-DF_c-densities of all five ligands; NMR spectra of the ligands; qNMR data. ITC-Titration Curves; amide CSPs and ^{15}N-T_2 relaxation per amino acid, synthesis protocols, analytic data,
This material is available free of charge via the Internet at http://pubs.acs.org.

AUTHOR INFORMATION

Corresponding Authors

* schwalbe@nmr.uni-frankfurt.de

* klebe@staff.uni-marburg.de

Author Contributions

B.W-S. performed expression, crystallization, crystal structure analyses and ITC, H.R.A.J., D.K. and S.S. expressed protein, measured CSP and ^{15}N-T_2-relaxation times, G.P. and C.L. contributed relaxometry measurements, T.W. performed the MD and GIST calculations, H.-D.G. synthesized the ligands, K.S., A.H., H.S and G.K. helped interpreting the data, all authors wrote the manuscript.

All authors have given approval to the final version of the manuscript.

Funding Sources

Funding was received from the European Research Council (ERC) awarded to G.K. and the LOEWE Research Cluster SynChemBio of the Federal State of Hesse (Germany).

Notes
The authors declare no competing financial interest.

ACKNOWLEDGEMENT

We acknowledge funding from the European Research Council (ERC) of the European Union, Project Number 268145 (DrugProfilBind) and the LOEWE Research Cluster SynChemBio of the Federal State of Hesse (Germany). Furthermore, we acknowledge support from and synchrotron beamtime at BESSY II Helmholtz-Zentrum Berlin in Berlin/Germany, and from Instruct-ERIC, a Landmark ESFRI project and, specifically, CERM/CIRMMP Italy centre. Computational resources and technical support were provided by HRZ Marburg.

ABBREVIATIONS

PKA: cAMP-dependent protein kinase, ITC: isothermal titration calorimetry, NMR: nuclear magnetic resonance spectroscopy, CSP: chemical shift perturbation, TROSY: Transverse relaxation optimized spectroscopy, MBT: Mes/Bis-Tris, DTT: Dithiothreitol, EDTA: Ethylenediaminetetraacetic acid, MPD: 2-Methyl-2,4-pentanediol, DMSO: Dimethyl sulfoxide, TEA: Triethanolamine, qNMR: quantitative nuclear magnetic resonance spectroscopy, PDB: protein data bank, PKI: protein kinase inhibitor, DFG: aspartat-phenylalanin-glycin motif, Gly: glycine, Ala: alanine, Asp: aspartate, Thr: threonine, Glu: glutamate; Arg: arginine, Ser: serine, Thr: threonine, Val: valine, Cys: cysteine, ATP: adenosine triphosphate,

REFERENCES

1 Freire, E. *Drug Discov Today* **2008**, *13*, 869–874.
2 Ladbury, J. E.; Klebe, G.; Freire, E. *Nat Rev Drug Discov* **2010**, *9*, 23–27.
3 Kawasaki, Y.; Freire, E. *Drug Discov Today* **2011**, *16*, 985–990.
4 Núñez, S.; Venhorst, J.; Kruse, C. G. *Drug Discov Today* **2012**, *17*, 10–22.
5 Klebe, G. *Nat Rev Drug Discov* **2015**, *14*, 95–110.
6 Ákos Tarcsay,; Keserü, G. M. *Drug Discov Today* **2015**, *20*, 86–94.
7 Mann, A. In *The Practice of Medicinal Chemistry*, second edition ed.; Wermuth, C. G., Ed.; Academic Press: London, 2003; pp 233 – 250.
8 Loughlin, W. A.; Tyndall, J. D. A.; Glenn, M. P.; Fairlie, D. P. *Chem Rev* **2004**, *104*, 6085–6117.
9 Chang, C. A.; Chen, W.; Gilson, M. K. *Proc Natl Acad Sci U S A* **2007**, *104*, 1534–1539.
10 Chaires, J. B. *Annu Rev Biophys* **2008**, *37*, 135–151.
11 Wong, C. F. *Biochim Biophys Acta* **2008**, *1784*, 244–251.
12 Huang, Z.; Wong, C. F. *J Comput Chem* **2009**, *30*, 631–644.

13 Kornev, A. P.; Taylor, S. S. *Trends Biochem Sci* **2015**, *40*, 628–647.
14 Olsson, T. S. G.; Williams, M. A.; Pitt, W. R.; Ladbury, J. E. *J Mol Biol* **2008**, *384*, 1002–1017.
15 Gilson, M. K.; Liu, T.; Baitaluk, M.; Nicola, G.; Hwang, L.; Chong, J. *Nucleic Acids Res* **2016**, *44*, D1045–D1053.
16 Manning, G.; Whyte, D. B.; Martinez, R.; Hunter, T.; Sudarsanam, S. *Science* **2002**, *298*, 1912–1934.
17 Shibuya, M.; Asano, T.; Sasaki, Y. In *Cerebral Vasospasm*; Seiler, R. W., Steiger, H.-J., Eds.; Springer Vienna: Vienna, 2001; pp 201–204.
18 Sasaki, Y.; Suzuki, M.; Hidaka, H. *Pharmacol Ther* **2002**, *93*, 225–232.
19 Breitenlechner, C.; Gassel, M.; Hidaka, H.; Kinzel, V.; Huber, R.; Engh, R. A.; Bossemeyer, D. *Structure* **2003**, *11*, 1595–1607.
20 Kudlinzki, D.; Linhard, V. L.; Saxena, K.; Sreeramulu, S.; Gande, S.; Schieborr, U.; Dreyer, M.; Schwalbe, H. *Acta Crystallogr F Struct Biol Commun* **2015**, *71*, 1088–1093.
21 Langer, T.; Vogtherr, M.; Elshorst, B.; Betz, M.; Schieborr, U.; Saxena, K.; Schwalbe, H. *Chembiochem* **2004**, *5*, 1508–1516.
22 Kabsch, W. *Acta Crystallogr D Biol Crystallogr* **2010**, *66*, 125–132.
23 McCoy, A. J.; Grosse-Kunstleve, R. W.; Adams, P. D.; Winn, M. D.; Storoni, L. C.; Read, R. J. *J Appl Crystallogr* **2007**, *40*, 658–674.
24 Adams, P. D. et al. *Acta Crystallogr D Biol Crystallogr* **2010**, *66*, 213–221.
25 Emsley, P.; Lohkamp, B.; Scott, W. G.; Cowtan, K. *Acta Crystallogr D Biol Crystallogr* **2010**, *66*, 486–501.
26 Laskowski, R. A.; MacArthur, M. W.; Moss, D. S.; Thornton, J. M. *J Appl Crystallogr* **1993**, *26*, 283–291.
27 Kleywegt, G. J.; Zou, J.-Y.; Kjeldgaard, M.; Jones, T. A. In *International Tables for Crystallography Volume F: Crystallography of biological macromolecules*; Rossmann, M. G., Arnold, E., Eds.; Springer Netherlands: Dordrecht, 2001; pp 353–356.
28 Smart, O. S.; Womack, T. O.; Sharff, A.; Flensburg, C.; Keller, P.; Paciorek, W.; Vonrhein, C.; Bricogne, G. http://www.globalphasing.com.
29 Bruno, I. J.; Cole, J. C.; Kessler, M.; Luo, J.; Motherwell, W. D. S.; Purkis, L. H.; Smith, B. R.; Taylor, R.; Cooper, R. I.; Harris, S. E.; Orpen, A. G. *J Chem Inf Comput Sci* **2004**, *44*, 2133–2144.
30 DeLano, W. L. *http://pymol. org* **2002**,
31 Keller, S.; Vargas, C.; Zhao, H.; Piszczek, G.; Brautigam, C. A.; Schuck, P. *Anal Chem* **2012**, *84*, 5066–5073.
32 Houtman, J. C. D.; Brown, P. H.; Bowden, B.; Yamaguchi, H.; Appella, E.; Samelson, L. E.; Schuck, P. *Protein Sci* **2007**, *16*, 30–42.
33 Masterson, L. R.; Shi, L.; Tonelli, M.; Mascioni, A.; Mueller, M. M.; Veglia, G. *Biomol NMR Assign* **2009**, *3*, 115–117.
34 Favier, A.; Brutscher, B. *J Biomol NMR* **2011**, *49*, 9–15.
35 Morikawa, A.; Sone, T.; Asano, T. *J Med Chem* **1989**, *32*, 46–50.
36 Makhija, M. T.; Kasliwal, R. T.; Kulkarni, V. M.; Neamati, N. *Bioorg Med Chem* **2004**, *12*, 2317–2333.
37 Goldberg, R. N.; Kishore, N.; Lennen, R. M. *J Phys Chem Ref Data* **2002**, *31*, 231.
38 Suárez, E.; Díaz, N.; Méndez, J.; Suárez, D. *J Comput Chem* **2013**, *34*, 2041–2054.
39 Nguyen, C. N.; Young, T. K.; Gilson, M. K. *J Chem Phys* **2012**, *137*, 044101.
40 Nguyen, C. N.; Cruz, A.; Gilson, M. K.; Kurtzman, T. *J Chem Theory Comput* **2014**, *10*, 2769–2780.
41 Velázquez-Muriel, J. A.; Rueda, M.; Cuesta, I.; Pascual-Montano, A.; Orozco, M.; Carazo, J.-M. *BMC Struct Biol* **2009**, *9*, 6.
42 Neeb, M.; Hohn, C.; Ehrmann, F. R.; Härtsch, A.; Heine, A.; Diederich, F.; Klebe, G. *Bioorg Med Chem* **2016**, *24*, 4900–4910.
43 Rühmann, E.; Rupp, M.; Heine, A.; Klebe, G. *ChemMedChem* **2016**, *11*, 309–319.
44 Martin, S. F.; Clements, J. H. *Annu Rev Biochem* **2013**, *82*, 267–293.

Insert Table of Contents artwork here

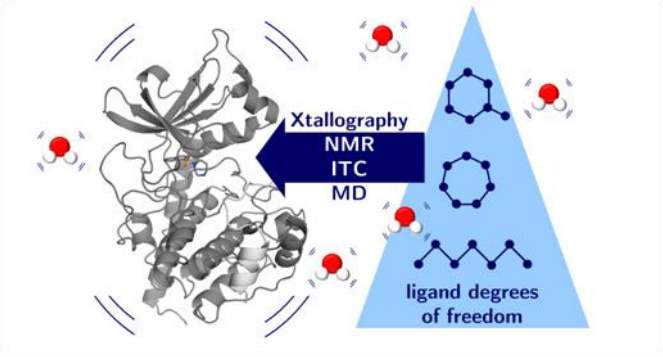
Xtallography
NMR
ITC
MD
ligand degrees
of freedom